materials

MDPI

Article

Investigation of Compressive and Tensile Behavior of Stainless Steel/Dissolvable Aluminum Bimetallic Composites by Finite Element Modelling and Digital Image Correlation

Xiuhui Li[1], Morteza Ghasri-Khouzani[1], Abdoul-Aziz Bogno[2], Jing Liu[2], Hani Henein[2], Zengtao Chen[1*] and Ahmed Jawad Qureshi[1*]

[1] Department of Mechanical Engineering, University of Alberta, Edmonton, AB T6G 1H9, Canada; xiuhui1@ualberta.ca (X.L.); ghasrikh@ualberta.ca (M.G.K.); zengtao@ualberta.ca (Z.C.); ajqureshi@ualberta.ca (A.J.Q)
[2] Department of Chemical and Materials Engineering, University of Alberta, Edmonton, AB T6G 1H9, Canada; bogno@ualberta.ca (A.A.B.); jing22@ualberta.ca (J.L.); hhenein@ualberta.ca (H.H.)
* Correspondence: zengtao@ualberta.ca (Z.C.); ajqureshi@ualberta.ca (A.J.Q.) [equal corresponding author]

Abstract: This study reports fabrication, mechanical characterization, and finite element modeling of a novel lattice structure based bimetallic composite comprised of 316L stainless steel and a functional dissolvable aluminum alloy. A net-shaped 316L stainless steel lattice structure composed of diamond unit cells was fabricated by selective laser melting (SLM). The cavities in the lattice structure were then filled through vacuum-assisted melt infiltration to form the bimetallic composite. The bulk aluminum sample was also cast using the same casting parameters for comparison. The compressive and tensile behavior of 316L stainless steel lattice, bulk dissolvable aluminum, and 316L stainless steel/dissolvable aluminum bimetallic composite and the comparison between experimental, finite element analysis (FEA) and digital image correlation (DIC) results, were investigated in this study. There is no notable difference in the tensile behavior of the lattice and bimetallic composite because of the weak bonding in the interface, so the load cannot be transferred from the 316L stainless steel lattice to the dissolvable aluminum matrix. However, the aluminum matrix is vital in the compressive behavior of the bimetallic composite. The dissolvable aluminum showed higher Young's modulus, yield stress, and ultimate stress than the lattice and composite in both tension and compression tests, but much less elongation. Moreover, FEA and DIC have demonstrated to be effective and efficient methods to simulate, analyze, and verify the experimental results through juxtaposing curves on the plots and compare strains of critical points by checking contour plots, respectively.

Keywords: selective laser melting (SLM); lattice structure; bimetallic composite; mechanical properties; finite element analysis (FEA); digital image correlation (DIC); hybrid manufacturing

Citation: Lastname, F.; Lastname, F.; Lastname, F. Title. *Materials* **2021**, *14*, x. https://doi.org/10.3390/xxxxx

Academic Editor: Firstname Lastname

Received: date
Accepted: date
Published: date

1. Introduction

Recently, lattice structures have attracted the attention of many researchers due to having properties such as lightweight, high strength, energy absorption, reducing material consumption and biocompatibility. Lattice structures are formed mathematically or geometrically by spatial arrangement and combination of a grouping of unit cells. Most researchers focus on the mechanical properties, such as compression and tension behavior [1–8], fracture behavior [9, 10], fatigue behavior [11, 12], and shear response [13], and biocompatibility [14–16] of these cells. Research has also been dedicated to the design method of the lattice structure, including creating functionally graded porous structures [4, 17–19], panel or sandwich-shaped lattice structures [20–22], and the mathematically designing algorithm [23–28].

Most work done on lattice structures has been about unit cells. Researchers were more likely to conduct experiments on normal unit cells formed by the spatial arrangements of struts. However, some of them shed light on complicated unit cells, whose composition components conform to specific mathematical algorithms, such as gyroid [1, 3, 5, 18, 19], Schwarz diamond [17, 29] called TPMS (triply periodic minimal surfaces), and plate lattices [25]. Compression and tension tests were applied in studying F2CC,Z (face-centered cubic with Z-struts), hollow spherical unit cells by Kohnen et al. [30], and concluded that the mechanical properties for F2CC,Z are better than hollow spherical. Contuzzi et al. [31] studied F2CC,Z structure, and compressive testing using two samples of different volume fractions and concluded that increasing strut thickness is more significant than introducing reinforcement in the lattice structure. Rehme et al. [32] investigated not only F2CC,Z, but also FCC (face-centered cubic) and F2BCC,Z (body-centered and face-centered cubic combined with Z-struts) structures. The difference between these three face-centered cubic unit cells can be seen in **Figure 1** (a), (b) and (e). BCC (body-centered cubic), BCC,Z (body-centered cubic with z-struts), gyroid and rhombic were also analyzed [2, 3, 12, 29, 33–35] through compressive, tensile, and fracture testing. They concluded that F2CC,Z has a higher load capacity, and gyroid can be very useful in applications requiring high stiffness. Peto et al. [36] and Park et al. [4] also gave an eye on other kinds of unit cells, which are relatively uncommon and not widely applied, and finally found that CD (cubic diamond) exhibited higher strength compared to others. An image of some unit cells mentioned above is shown in **Figure 1**, and all of them are self-supported for 3D printing except FCC and CD.

Among all unit cells, diamond unit cells are considered the best choice for structures with strength requirements. With predictions of the Gibson-Ashby model, research done by Maconachie et al. [29] evidenced that diamond lattice structures exhibit larger relative strength and relative modulus in the same volume fraction of lattice. However, traditional diamond unit cells, namely CD unit cells, are not self-supported, which might cause some problems in fabrication through additive manufacturing; hence, another type of diamond unit cell inspired by ANSYS Space Claim™ is plotted in **Figure 1** (h). This new sort of diamond unit cell was shown in the lattice auto-generating feature in the Space-Claim, yet researchers have never investigated it. Moreover, many studies have already been conducted on normal unit cells such as BCC and F2CC,Z, so this new sort of diamond unit cell is novel enough, and can also be considered as a breakthrough point in contemporary research of lattice structures. Consequently, this diamond unit cell was chosen for the lattice structure in our study.

Moreover, the manufacturing method of lattice structure has also received widespread attention, and a popular one nowadays should be metal 3D printing, which is also named metal additive manufacturing (MAM). MAM can directly print a sample on a panel from the bottom to up by metal material feedstock. The sample can be achieved from a computer-aided design (CAD), although there are some limitations of samples to be printed in terms of size and geometry for different machines. Selective laser melting (SLM) is one of the categories of MAM. In SLM, thin layers of atomized fine metal powder are evenly distributed using a coating mechanism onto a substrate plate. Then, each layer of the part geometry is fused by selectively melting the powder, which is achieved with a high-power laser beam. Despite this, some researchers tried to investigate the defects of the structure fabricated by SLM or AM (additive manufacturing) even if it is prevalent nowadays. It was noted that struts waviness, strut oversizing or strut thickness variation could be found on lattice structures by SLM [9, 37–41], and horizontal struts feature more severe geometric imperfections than vertical struts and diagonal struts [9, 39, 41, 42]. Moreover, vertical struts are thinner than as-designed ones [9, 37, 39], and the magnitude of strut oversizing can change the failure mode from one to another [9]. SLM parameters will also affect the mechanical properties of lattice structures [3, 43]. Horizontal struts are the first to fracture, indicating they are experiencing greater stress than neighboring struts [41, 44], which reminded us of the printing orientation of our samples.

Although there are some flaws in the structure fabricated by SLM, evidence showed that SLM lattice structures manufactured from stainless steel powder have excellent mechanical performance [32]. Microstructural and mechanical characterizations of duplex stainless steel UNS S31803 processed by SLM was conducted by Hengsbach et al. [45], and validated the successful fabrication of duplex stainless steel processed via SLM. Not only duplex stainless steel, but 316L stainless steel also has been favored by researchers. Mechanical properties and deformation behavior of 316L lattice structures fabricated by SLM were studied [30, 46], as well as fracture toughness [3]. Then, bimetallic lattice composite slowly entered the sight of researchers. The lattice composite contains two parts, namely the lattice part, as well as the matrix part, in which another material is filled into the lattice gaps, and bimetallic means the metal feedstock created both two parts. There is also much research on the microstructure and mechanical properties of bimetallic lattice structures manufactured by SLM, such as CuSn/18Ni300 bimetallic porous structures [47], and A356/316L interpenetrating phase composites [48, 49], in which [49] investigated the mechanical properties of PrintCast composites through finite element analysis (FEA), coupled with digital image correlation (DIC) to capture the deformation and failure processes.

FEA is commonly used for simulating the experimental process and validating testing results. Researchers usually conducted FEA for performance evaluation [50–52], structure design [53], investigating configurational effects [54], and studying the failure mechanism [55, 56]. However, DIC system was not widely applied to experiments of metal lattices. Digital image correlation (DIC) is a 3D, full-field, non-contact optical technique to measure contour, deformation, vibration, and strain on almost any material. DIC setting is essential for investigating strain rate by analyzing captured images, and it is also apparent to show elongation changing along with the experiments processing. Limited research was done for analyzing deformation and strain evolution applying DIC on stainless steel such as 316L [30, 49, 57]. Mostly, they were more concentrated on studying titanium alloy Ti6Al4V [58–61]. Other investigations on displacement, velocities, and stress measurements using DIC were also done on polymers [62], glass fibers [63], and other materials [64, 65].

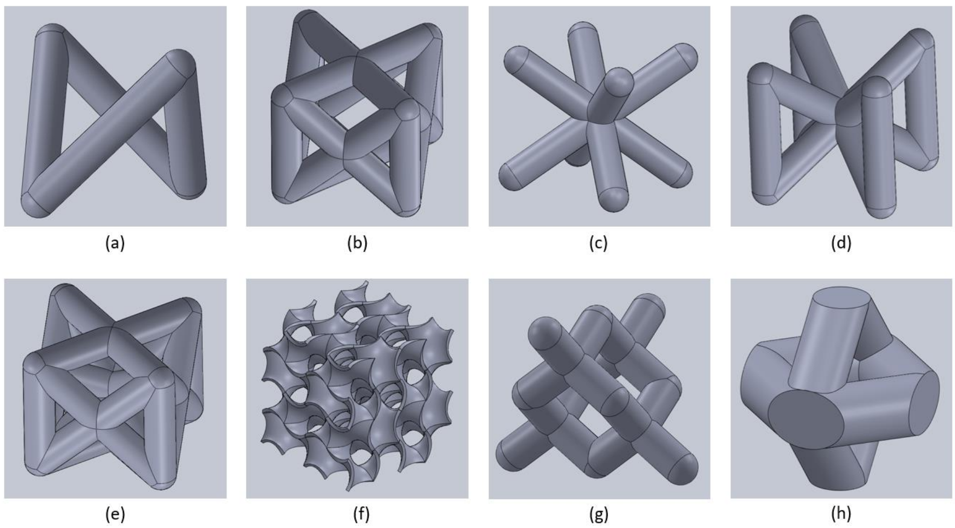

Figure 1. Unit cells in lattice structures: (**a**) FCC; (**b**) F2CC,Z; (**c**) BCC; (**d**) BCC,Z; (**e**) F2BCC,Z; (**f**) gyroid; (**g**) CD; (**h**) Ansys Space-Claim™ diamond.

In this study, FEA and DIC's mechanical properties of 316L stainless steel/dissolvable aluminum bimetallic composites are investigated, which are vital for simulating and recording experimental processes. 316L stainless steel lattice structures formed by the unit cell shown in **Figure 1** (h) were built using the SLM method, and a molten aluminum alloy infiltrated the 316L stainless steel lattice gaps to create the bimetallic composite.

Mechanical properties were analyzed thoroughly by both tension and compression tests, and the experimental results were compared with those from FEA to validate its effectiveness. Simultaneously, the DIC system was also applied to capture strain distribution and verify the FEA results. The following section provides the details of materials and methods used. Section three describes the FEA simulation model and experimental validation for individual lattice an, filler structure. This is followed by section four which provides the details on the FEA simulation and experimental validation of bimetallic composite strcutures. Finally, the last section, five, provides conclusions.

2. Materials and Methods

2.1. Manufacturing

To better study the mechanical properties of materials and structures, both compression and tension tests needed to be performed. Hence, bulk samples, lattice samples and bimetallic composite samples were required for both tension and compression tests. 316L stainless steel was selected for creating the lattice by SLM method, while aluminum was for the filled-in matrix part of composite by casting. Besides, bulk aluminum samples were also fabricated by casting.

Compression samples of lattice were in the shape of a cube with a length of 12.5 mm, while the tension samples of lattice were a dog-bone shape, whose dimensions conformed to ASTM E8M standard [66], with a gauge length of 50 mm and gauge width of 12.5 mm. The strut diameter of the lattice structure unit cell is the same for both the compression and tension samples, which is 2 mm. Failure of the tension samples should occur in the gauge zone rather than the interface between the diamond lattice part and the solid gripping part, which is the location of stress concentration. Therefore, fillets were required on the junction interface to reduce the concentrated stress and avoid failure in this area. The 0.75 mm fillets of the tension sample and the compression sample are displayed in Figure 2. The chemical composition of gas atomized 316L stainless steel powder for the SLM process is listed in Table 1. An EOS M290 machine manufactured diamond lattice structure parts with a Yb-fiber laser. Tension lattice dog-bone samples were fabricated in a horizontal orientation to the building plate (a hot-rolled mild steel panel with a dimension of 252 mm × 252 mm × 25 mm). EOS Company recommended processing parameters were applied for the 316L stainless steel, and the detailed parameters are listed in [67].

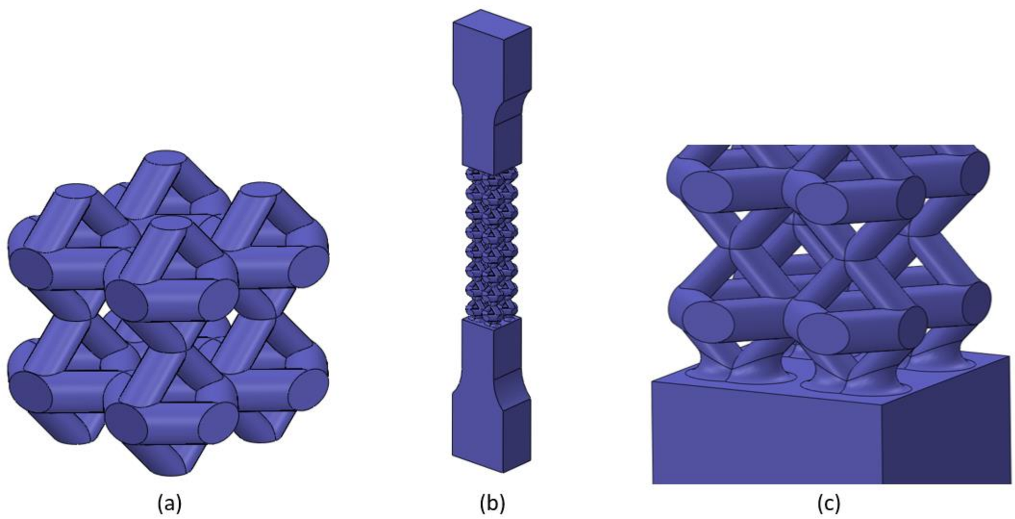

Figure 2. CAD models of the Space-Claim diamond lattice structure parts: (**a**) compression model; (**b**) tension dog-bone model; (**c**) fillets in the interface of dog-bone model.

Table 1. Chemical composition of 316L stainless steel powder used as the feedstock material for the AM process (wt. %).

C	Cr	Mn	Mo	N	Ni	O	S	Si	Fe
0.03	17.9	2.0	2.4	0.1	13.9	0.04	0.01	0.75	Balance

Bimetallic composite samples were manufactured based on the lattice ones. For both compression and tension composite samples, dissolvable aluminum was filled into the lattice structure gaps and formed a matrix part of the composite by the casting process. The chemical composition of dissolvable aluminum was clarified in **Table 2**, and the details for the casting process were illustrated in Section 2.2 of [67]. Bulk aluminum samples were also fabricated under the same casting condition.

Microstructure analysis for the specimens can be found in Section 2.3 of [67]. An image of all the experimental samples is presented in **Figure 3**.

Table 2. The chemical composition of the aluminum alloy used for casting (wt. %).

Fe	Ag	Ga	Cu	Mg	Al
0.6	2.1	2.0	2.6	4.1	Balance

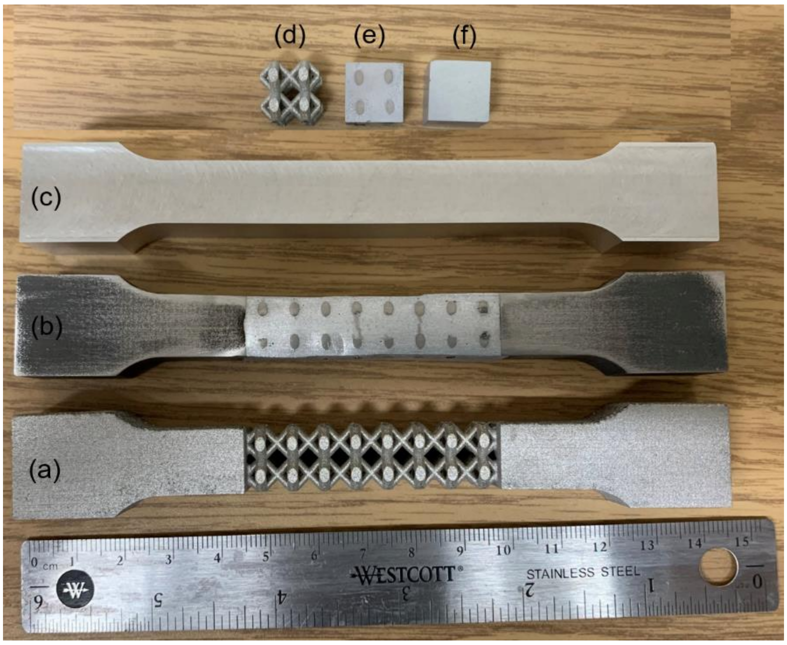

Figure 3. An image of the experimental samples: (**a**) stainless steel lattice dog-bone; (**b**) stainless steel/aluminum composite dog-bone; (**c**) bulk aluminum dog-bone; (**d**) stainless steel lattice cube; (**e**) stainless steel/aluminum composite cube; (**f**) bulk aluminum cube.

2.2. DIC system setting

In our experiments, VIC-Snap commercial software (manufactured by Correlated Solutions, Inc.) was used to capture images, and VIC-3D 8 commercial software (manufactured by Correlated Solutions, Inc.) was applied to process the images.

Two Allied Vision Technology (AVT) Pike F421b cameras (resolution of 2048 (H) X 2048 (V), sensor size: type 1.2), equipped with two Nikon 28-85 mm F-mount lenses by two C to F-mount adapters(for lenses), which allows adjusting aperture, focus, and zoom, were mounted on a tripod and used in the experiments. Both two lenses provide an average magnification of 10 pixel/mm. One of the cameras was precisely positioned with its lens perpendicular to the focused surface of the lattice sample during the experiments.

The other camera's lens was positioned at 25° to the primary camera. The testing images were captured one frame per second, with each frame capturing a compression displacement at around 8 microns and a tension displacement around 33 microns according to the loading speed of 0.5 mm/min and 2 mm/min, respectively. The specimens were sprayed with black and white paint to form a scattered speckle pattern on the focused surface with an average diameter of speckles of about 1.3 mm (approximately 5 pixels).

Before capturing testing images, a calibration target card with 8X8 dots was imaged simultaneously by rotating to different angles in both cameras to calibrate the system in one step thoroughly.

2.3. Mechanical testing

Uniaxial compression and tension tests at room temperature were conducted on all the experimental specimens. The displacement-controlling mode was applied on all the tests using a servo-hydraulic mechanical testing system (MTS 810). The cross-head speed was 0.5 mm/min for compression tests and 2 mm/min for tension tests, leading to an initial strain rate of 6.67310-4 s-1 for both compression and tension experiments. For more details of the mechanical testing, please refer to Section 2.4 of [67].

3. FEA simulation and experimental validation of individual lattice, and bulk structures

3.1. FEA procedure

The FE analysis was conducted using the commercial FE code ABAQUS/Explicit (2019 version) [68], with simulation models generated using SolidWorks [69]. Comparing to ABAQUS™/Standard, ABAQUS™/Explicit solver can better solve the convergent problems for models with complex configurations, especially for lattice structures. Furthermore, it can also readily analyze problems with complicated contact interaction between the independent bodies [49] for the bimetallic lattice structures clarified in Section 4.

The simulation model needs to be imported into ABAQUS before conducting the FE analysis. Then, the material parameters such as Young's modulus, Poisson's ratio for elasticity, and "true stress" vs. "plastic strain" values for plasticity in the ABAQUS property-material module are setup. The plasticity "true stress" vs. "plastic strain" pairs of values for 316L stainless steel was obtained from [70], while data for aluminum was obtained from the bulk aluminum experiments. After setting up the materials, assigning the specific material to the model configuration accordingly, for example, 316L stainless steel was given to the lattices while aluminum to the bulk aluminum models.

For compression model boundary conditions, the bottom end (one surface for bulk models, four small surfaces for lattice models) was fixed for all the six degrees of freedom (U1=U2=U3=UR1=UR2=UR3=0). Simultaneously, a reference point was generated on the top and coupled with the top end (one surface for bulk models, four small surfaces for lattice models), with five degrees of freedom fixed (U1=U3=UR1=UR2=UR3=0) and one remained (U2) for the loading. A velocity of 0.5 mm/min was then applied to the top reference point in the U2 direction. Note that the applying velocity should not be consistent from the beginning of the analysis until the end. Based on the actual experiment, the loading speed shall change gradually from 0 at first to the maximum in the middle, then dropped back to 0 in the end, in which the average rate would be 0.5 mm/min. In this case, the amplitude of velocity gradually changed throughout the whole loading process. As for tension models, similarly, the bottom end of the dog bone gripping area was fixed for all degrees of freedom (U1=U2=U3=UR1=UR2=UR3=0), while a velocity of 2 mm/min was applied to the reference point on the top in the U2 direction (U1=U3=UR1=UR2=UR3=0).

The last step before running the FE analysis was meshing. The free linear tetrahedral 3D stress element (C3D4 element type) was selected for both compression and tension lattice models and tension bulk dog bones, while the structured linear hexahedral 3D stress element (C3D8 element type) without reduced integration for compression bulk samples. Note that C3D4 was also used on the gripping block areas of tension lattice models to assure consistency with the lattice part. The mesh size for compression lattice samples is 0.5 mm, while 1 mm for all other models. For the compression bulk 316L stainless steel model, the compression bulk aluminum model, and the 316L stainless steel lattice model, the numbers of elements are 2197, 2197 and 47336, respectively, with node numbers of 2744, 2744, and 10895. For the tension bulk 316L stainless steel model, tension bulk aluminum model, and tension 316L stainless steel lattice model, the numbers of elements are 158001, 158001, and 188681, respectively, with nodes numbers of 30622, 30622, and 40588.

Figure 4 and Figure 5 show deformation contour plots for bulk 316L stainless steel, bulk aluminum, and 316L stainless steel lattice under both compressive and tensile conditions. Stresses shown in the plots were all Von-Mises stress averaging at 75%. The value 75% here means if the relative difference between contributions that specific node gets from neighboring elements is less than 75%, these contributing values are averaged [68]. It is evident that 316L stainless steel is much stronger and can afford more stress than aluminum under both compressive and tensile conditions. Moreover, compressive strength is almost the same as tensile strength for the lattice sample since there is no significant difference between their ultimate stress in the deformed contour plots.

After getting the contour plot, the reaction force and displacement of the top reference point of each model were exported from ABAQUS to an excel sheet. The engineering stress (σ_E) and engineering strain (ε_E) were obtained using the equations below:

$$\sigma_E = \frac{The\ \ reaction\ \ force\ \ (N)}{The\ \ failure\ \ cross\ \ section\ \ area\ \ (mm^2)} MPa \tag{1}$$

$$\varepsilon_E = \frac{The\ \ displacement\ \ (mm)}{The\ \ sample\ \ (gauge)\ \ length} \tag{2}$$

The compression model is a cube of 12.5 mm in each direction, and the gauge length for all tension models is 50 mm. The cross-section area for both compression and tension bulk models is 156.25 mm^2 (12.5 mm × 12.5 mm). However, as the cross-section area varies throughout the whole length of lattice samples, the average cross-section area size of 60.99 mm^2 is adopted with a maximum of 109.42 mm^2 and a minimum of 12.56 mm^2. Figure 6 shows the positions of maximum and minimum areas of the lattice using the compression one as the example.

Using the formulas below, we can convert the engineering stress (σ_E) and engineering strain (ε_E) to true stress (σ_T) and true strain (ε_T):

$$\varepsilon_T = \ln(1 + \varepsilon_E) \tag{3}$$

$$\sigma_T = \sigma_E(1 + \varepsilon_E) \tag{4}$$

The "true stress" vs. "true strain" plots for FE compression and tension tests are shown in Figure 7 and Figure 8. The experimental work will be discussed in Section 3.2, and the comparison will be made between the FEA and experimental results to verify the consistency.

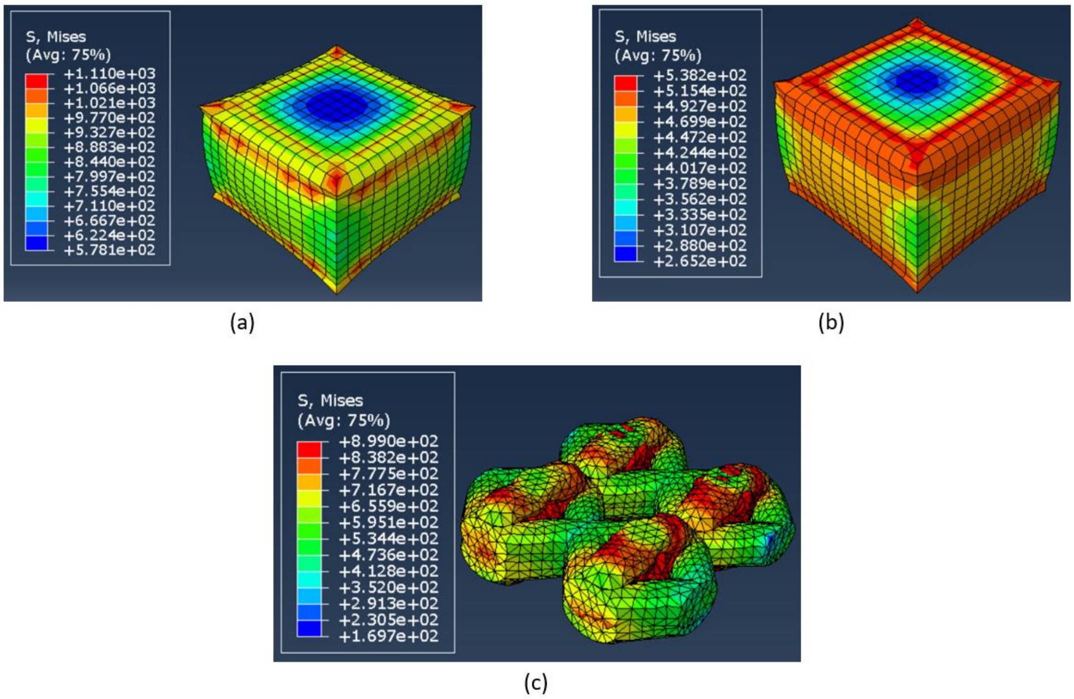

Figure 4. Deformation contour plots of FEA for compression samples: (**a**) bulk 316L stainless steel cube; (**b**) bulk dissolvable aluminum cube; (**c**) 316L stainless steel lattice.

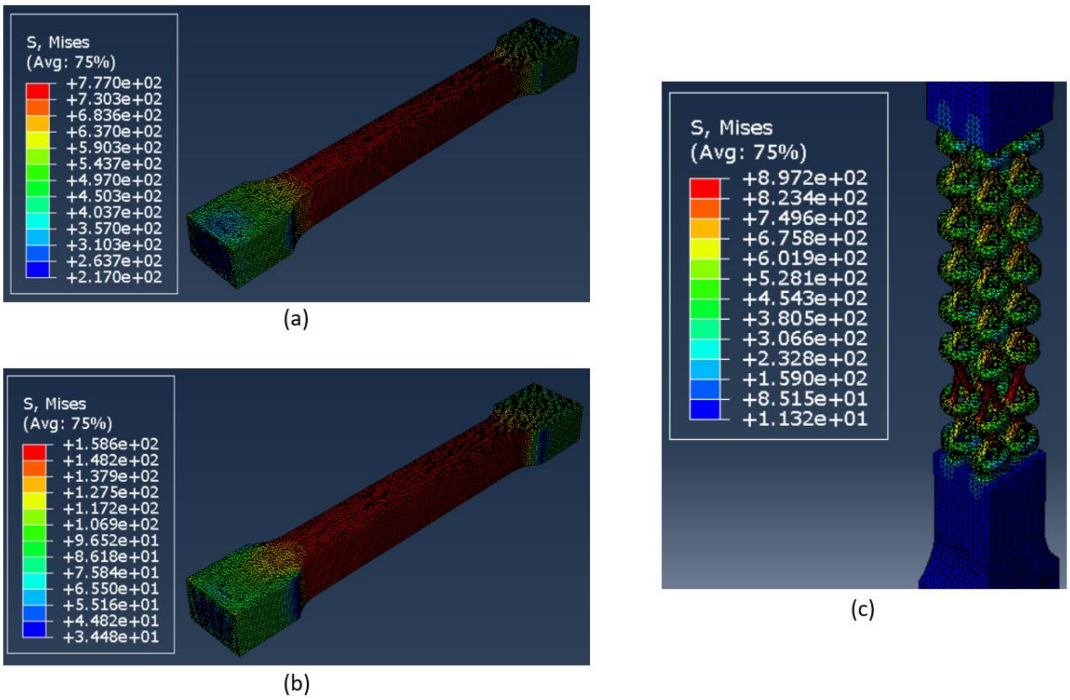

Figure 5. Deformation contour plots of FEA for tension samples: (**a**) bulk 316L stainless steel dog-bone; (**b**) bulk dissolvable aluminum dog-bone; (**c**) 316L stainless steel lattice dog-bone.

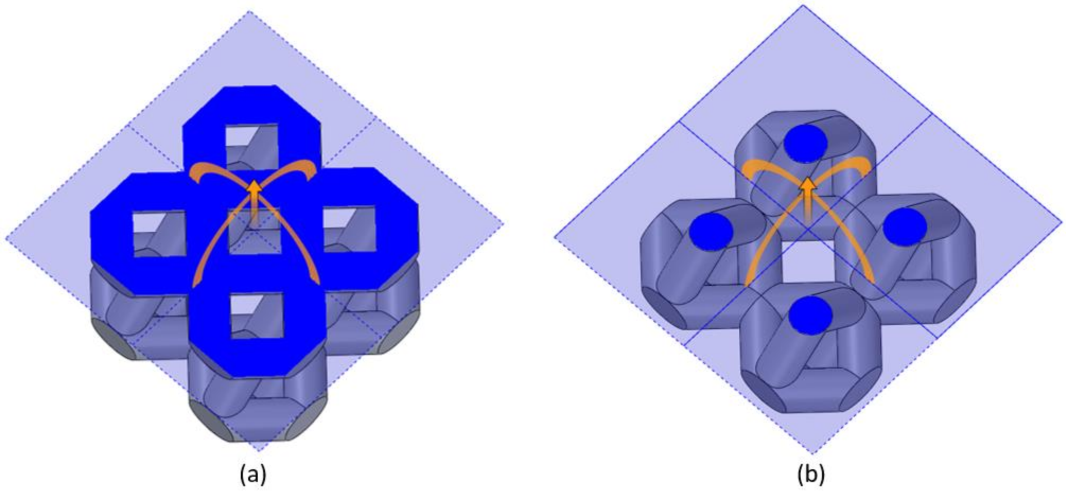

Figure 6. Maximum and minimum areas of the compression lattice model: (**a**) maximum area and (**b**) minimum area.

3.2. Experimental validation of FEA results

The experimental 316L stainless steel data was obtained from [70]. Overlapping the FEA compression plot in Section 4.1 to this experimental plot, we then obtained the final comparison plot between the FEA result and experimental result for all bulk and lattice specimens shown in **Figure 7**. We can see that for the three materials, the FEA results and experimental results are in conformance with each other, with average calculated numerical deviations of 9.8% and 5.0% for yield stress and ultimate compressive stress, respectively. However, it is also obvious that the yield and ultimate compressive stress of 316L stainless steel lattice are less than those of both the bulk aluminum and the bulk 316L stainless steel, which means the strength of the lattice with a volume fraction of 28.82% is significantly less than the solid samples due to low volume fractions. The ultimate compressive stress, which represents the compressive strength of the lattice, can be significantly enhanced by increasing the lattice strut diameter [31]. Furthermore, the cracks in the microstructure of the lattice can also explain the much lower yield stress and compressive strength.

Moreover, **Figure 7** shows that the compression test for bulk aluminum stopped much earlier than the 316L stainless steel lattice counterpart. This is due to the test being stopped at the load limit (100kN) of the mechanical testing machine before the specimen failure, while the 316L stainless steel sample collapsed before the test stopped. Three significant deformation stages, which are the elastic stage, plateau stage and densification stage, are shown in the 316L stainless steel compressive curve compared with the bulk aluminum. Initially, lattice struts were in an elastic deformation stage under the compressive load. Then, the struts approached the yield point, and the plastic stage began, which is indicated as the plateau stage. In the plateau stage, the strut nodes were dramatically squeezed, and plastic hinges formed. Finally, the densification started since the struts were continuously compressed to the point where some were broken, while others were closely squeezed against each other.

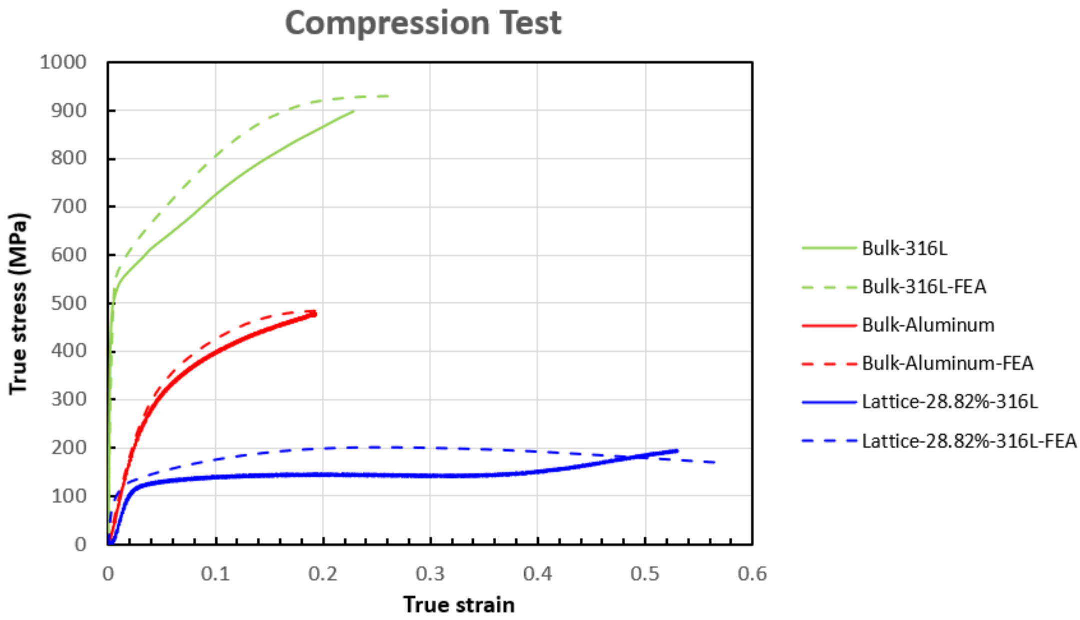

Figure 7. Comparison between experimental and FEA results of bulk 316L stainless steel, bulk dissolvable aluminum, and 316L stainless steel lattice for the compression test.

Identically, the experimental 316L stainless steel data was also collected from [70]. In order to be consistent with the compression result and further compare with the FEA result, all the experimental engineering values were transformed to the true values by using Eqs. (3) and (4). Similarly, mapping the FEA tension plot in Section 4.1 to this experimental plot, we then obtained the final tension plot between the FEA result and experimental result for all bulk and lattice specimens shown in Figure 8. This plot also validates that the FEA results agree with the experimental, with average calculated numerical deviations of 2.1% and 8.9% for yield stress and ultimate tensile stress. Likewise, the yield stress and tensile strength of the 316L stainless steel lattice are much lower than the other two bulk models. Increasing the strut diameter to achieve a bigger volume fraction will also improve the tension property.

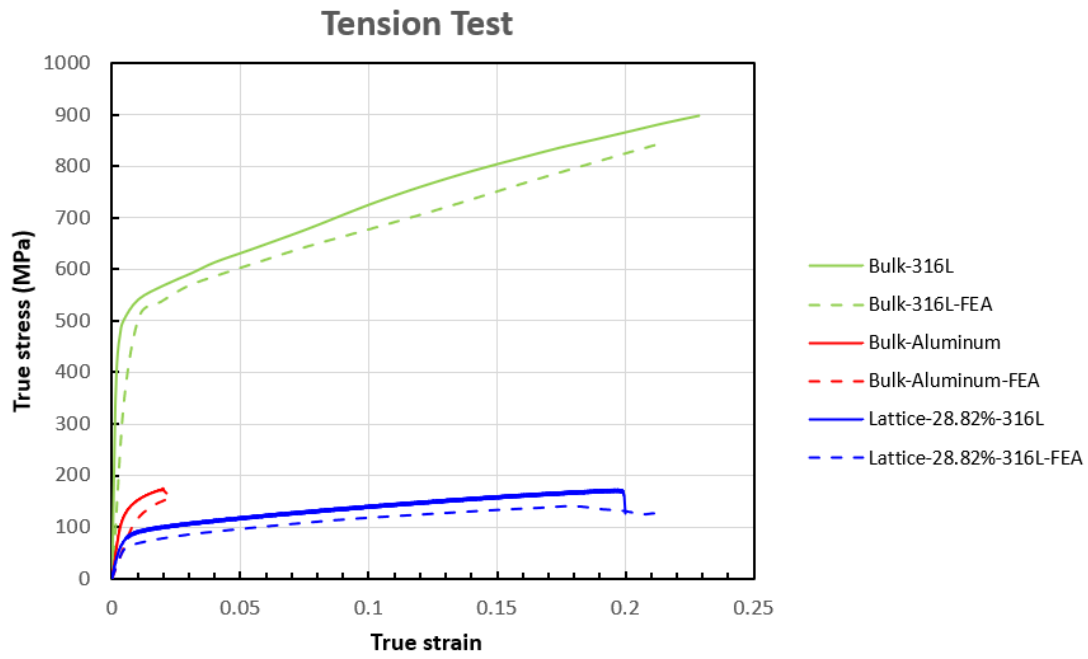

Figure 8. Comparison between experimental and FEA results of bulk 316L stainless steel, bulk dissolvable aluminum, and 316L stainless steel lattice for the tension test.

Unlike the compression testing, which has three deformation stages, the 316L stainless steel lattice just experienced the initial elastic stage and the elongational plastic stage, followed by fracture failure with a sudden drop in stress eventually. Moreover, the tensile behavior of the bulk aluminum exhibits an apparent difference from the other two, with a higher Young's modulus than the lattice but much less elongation than the other two. This is because aluminum is more brittle and has lower resistance to the tensile loading than 316L stainless steel, making it much easier to fracture with shorter elongation. In contrast, the diamond lattice configuration achieved a much-extended elongation and can be widely used in the energy absorption structure.

3.3. Experimental validation with DIC results

As for the comparison between the experimental and DIC results, we discuss the compression bulk aluminum and tension 316L stainless steel dog-bone lattice samples for brevity. A detailed view of bulk aluminum compression experimental curve is shown in Figure 9. Three unique points, namely the yielding point, the point in the plastic region, and the point in the hardening region, were marked out with their true strain and true stress values. The corresponding DIC images to these points are shown in Figure 10.

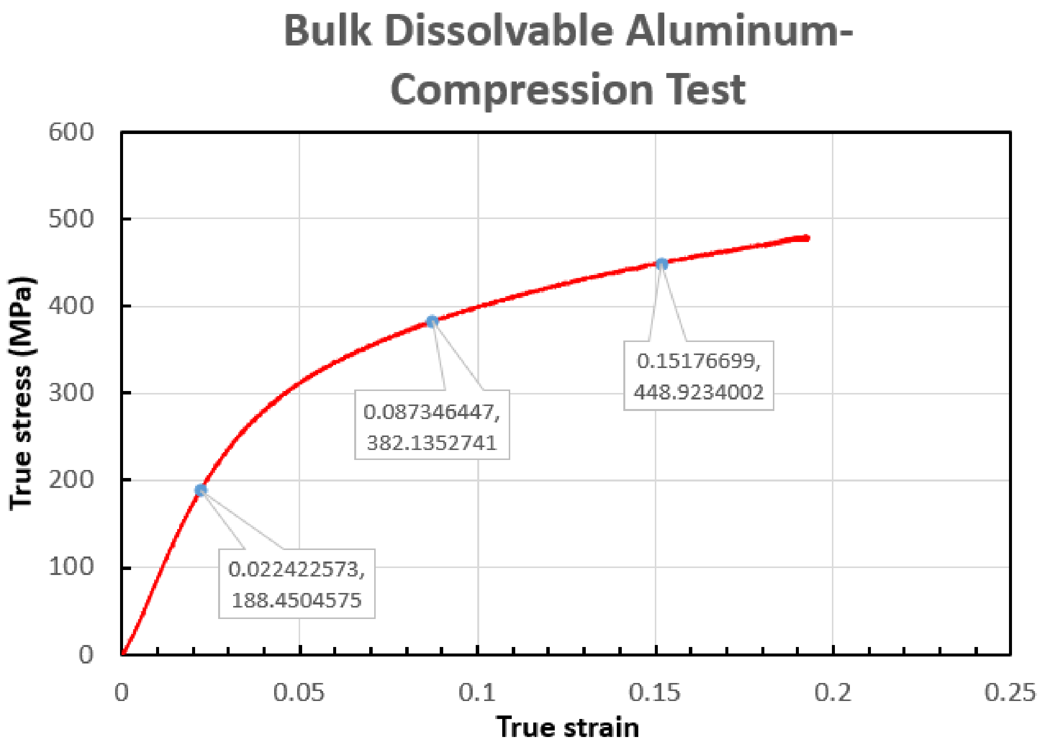

Figure 9. The experimental result of compression bulk dissolvable aluminum cube with three unique points marked out with *true stress* and *true strain*.

The scale bar is listed on the right side of each picture, with the strain range of -0.2 to 0 (negative values represent the compression test). From the frames, we can see that the color symbolizing engineering strain changes with loading progression, and the experimental results match the value range as the frames plotted.

Similarly, four particular points, namely the yielding point, the turning point, the point in the plastic region, and the point before the curve drop, are marked out on the tension test experimental curve of the 316L stainless steel dog-bone lattice in **Figure 11**. with corresponding DIC images shown in **Figure 12** in an increasing strain sequence with strain ranging from 0-0.2.

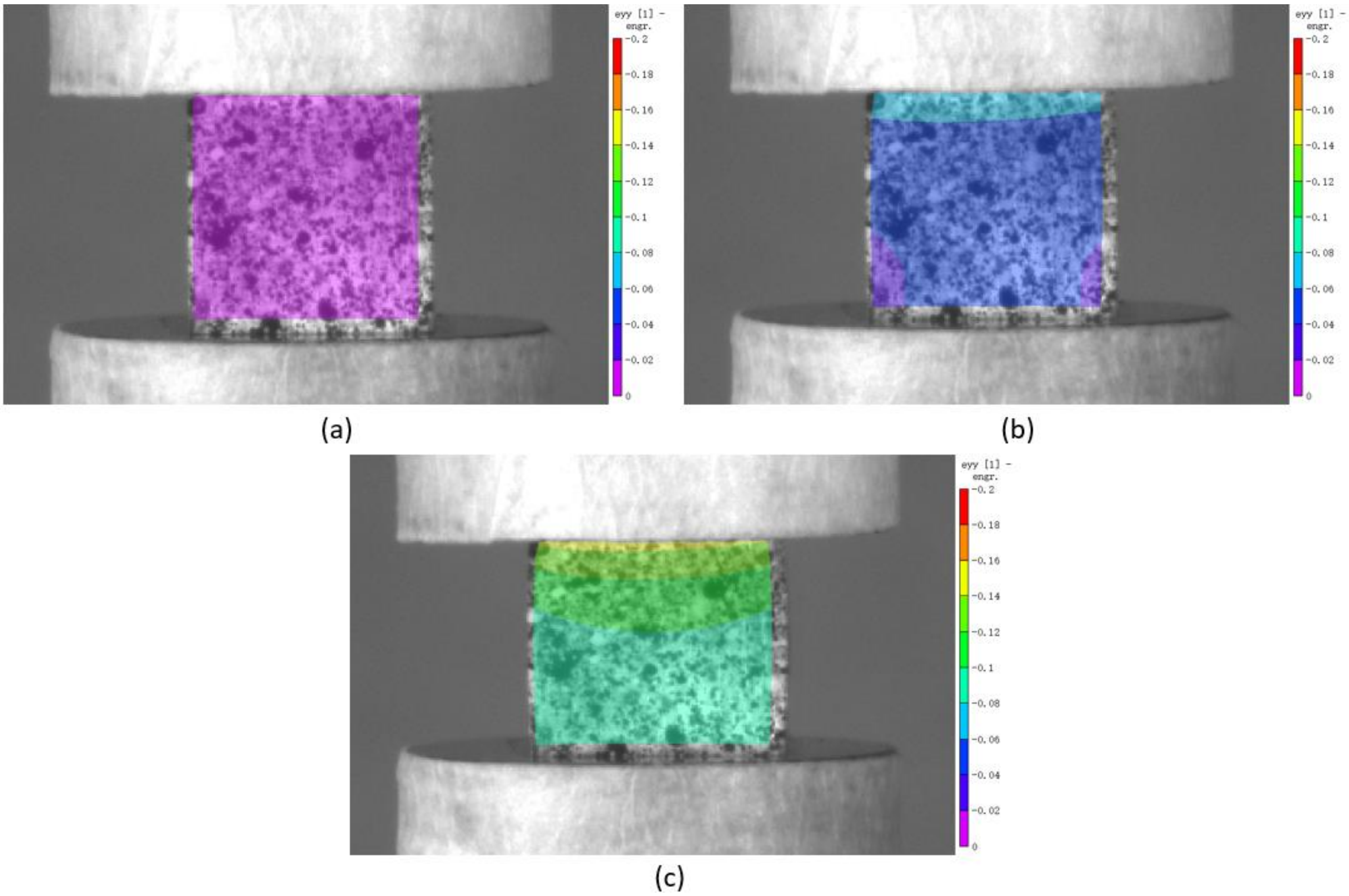

Figure 10. DIC frames of the three points marked out in the bulk dissolvable aluminum compression curve: (**a**) 34 s; (**b**) 131 s; (**c**) 228 s.

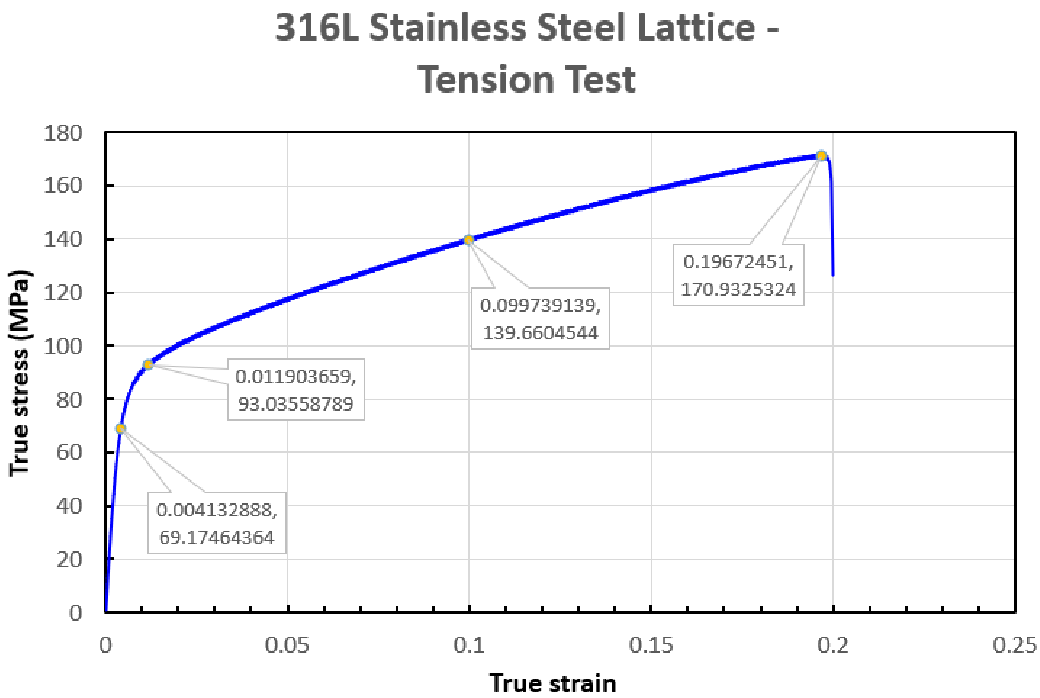

Figure 11. The experimental result of tension 316L stainless steel dog-bone lattice with four unique points marked out with *true stress* and *true strain*.

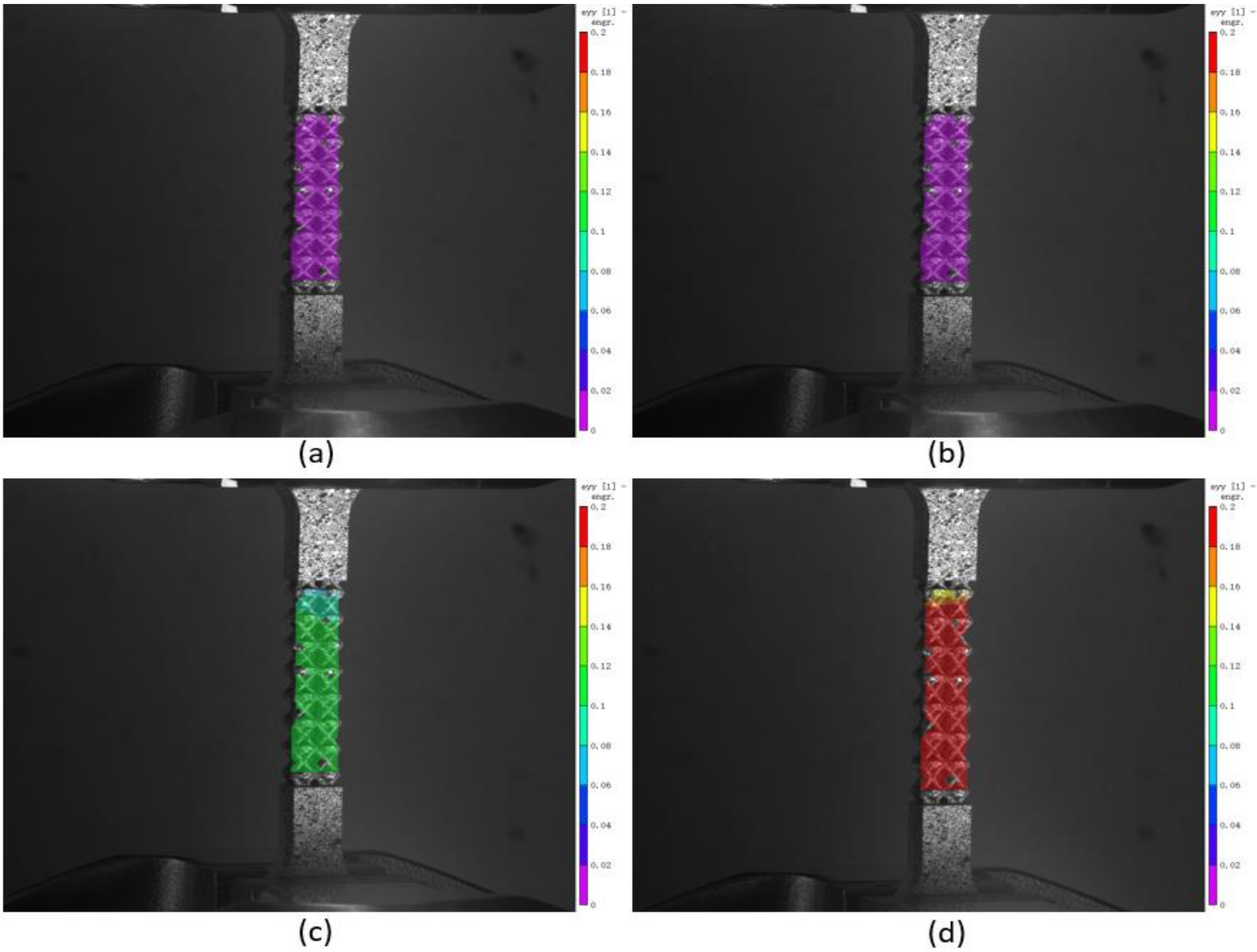

Figure 12. DIC frames of the four points marked out in the tension 316L stainless steel dog-bone lattice curve: (**a**) 6 s; (**b**) 18 s; (**c**) 150 s; (**d**) 295 s.

4. FEA simulation and experimental validation of bimetallic SS316L-Aluminum alloy bimetallic composite

4.1. FEA procedure

For FEA modeling of the bimetallic composite, two separate models were constructed in SolidWorks™ and imported and combined in ABAQUS™. ABAQUS™/Explicit (2019 version) solver was used in this work as it is appropriate to solve problems of two models contacting each other. Separate models of both compression composite and tension composite created in SolidWorks are shown in Figure 13.

Similar to procedure in Section 3.1, the materials were assigned to the corresponding part of the composite after importing the models into ABAQUS™. Materials for both compression composite and tension composite are the same, namely 316L stainless steel for the lattice part and aluminum for the filled-in matrix part. Next, separate models were assembled into one composite pattern, and the geometry centers of both the lattice part and the matrix part were ensured to coincide. Setting up interaction between two objects of a composite is critical in ABAQUS FEA. Based on the microstructural analysis of the interface as reported in [67], it is observed that there is no cohesive bonding between the two parts, and therefore, a "hard contact" interaction of the 316L/aluminum interface was generated in ABAQUS. Two surface sets were established, with one set of the outer surfaces of the lattice, and the other of the inner surfaces of the matrix, to be selected for creating the surface interaction. No penetration in the normal direction is assumed, and isotropic friction with a coefficient of 0.3 in the tangential direction is applied without elastic slip and any other shear stress for both the compression and tension composite patterns. Finally, a reference point is created on the top surface and coupled with the top cover for applying the load.

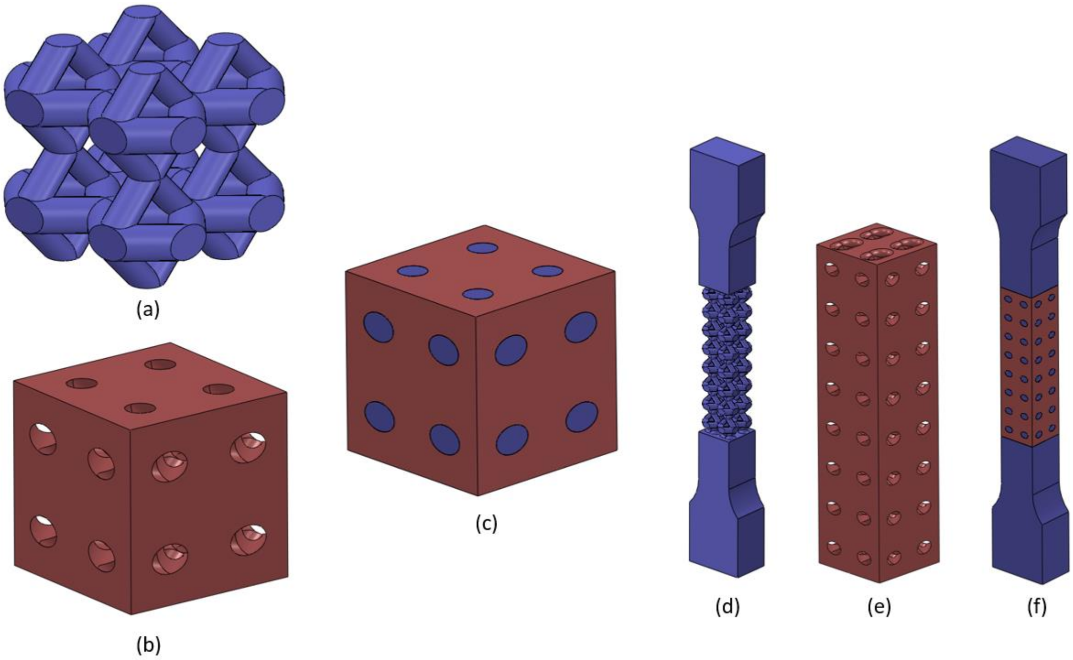

Figure 13. CAD models of the composite parts: (**a**) lattice part for the compression composite; (**b**) matrix part for the compression composite; (**c**) the compression composite; (**d**) lattice part for the tension composite; (**e**) matrix part for the tension composite; (**f**) the tension composite.

The boundary conditions for both compression and tension composites are the same as the models for bulk and lattice experiments. The bottom end was fixed for all the six degrees of freedom (U1=U2=U3=UR1=UR2=UR3=0), and the top reference point was held for five degrees of freedom except for U2 (U1=U3=UR1=UR2=UR3=0). A gradually changed velocity of an average of 0.5 mm/min was applied on the reference point for the compression sample, while 2 mm/min for the tension, maintaining consistency with the experiments. Figures of boundary conditions for compression and tension composites are omitted here since there is no significant difference with those shown in Section 3.1.

The free linear tetrahedral 3D stress element (C3D4 element type) was applied to both the lattice and matrix part of compression and tension composites. It is worth noting that the gripping block areas of the tension composite dog-bone also used C3D4, which is identical to the tension lattice dog-bone meshing. The mesh size for the compression composite was 0.5 mm, while 1 mm for the tension composite. Moreover, there are overall 152845 and 327547 elements, and 32891, and 70978 nodes for the whole compression and tension composites, respectively.

Figure 14 gives the deformation contour plots of two composites. Stresses shown in the plots were all Von-Mises stress averaging at 75% of elongation. We can see that the composite is severely deformed under the compressive loading, and the matrix part is in light-green colour, which means it afforded the load and played an essential role in resisting the load. In contrast, the tension composite matrix is almost in the blue colour. Compared with the scale bar, we know that the insignificant load transferred to the matrix. This is due to a lack of interface fusion due to continuous cracks in the 316L/aluminum interface preventing the load transfer from the lattice to the matrix.

"Engineering stress" and "engineering strain" were then collected from the reaction force and displacement exported from ABAQUS using Eqs. (1) and (2), and corresponding "true stress" and "true strain" were calculated by Eqs. (3) and (4). The sample length was 12.5 mm for the compression composite, while 50 mm (gauge length) for the tension composite. The cross-section area was 156.25 mm^2 (12.5 mm × 12.5 mm) for the compression; however, it is not that case for the tension.

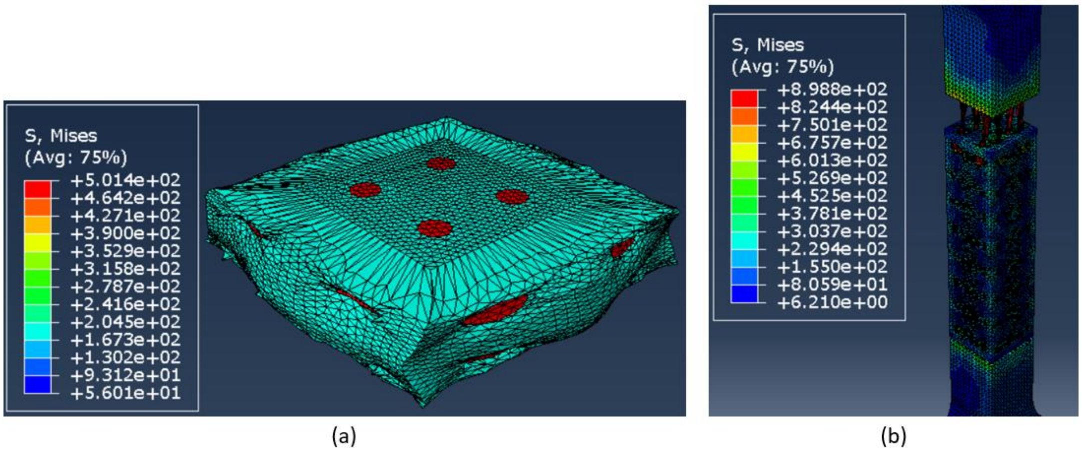

Figure 14. Deformation contour plots of FEA for composite samples: (**a**) compression composite cube and (**b**) tension composite dog-bone.

The "true stress" vs. "true strain" plots for compression and tension composite FEA results are shown as dashed black lines in Figure 15 and Figure 16, respectively in Section 4.2 for comparison. Similarly, the experimental work will also be discussed, and the comparison will be made between the FEA and experimental results to verify the consistency.

4.2. Experimental validation of FEA results

"True stress" vs. "True strain" curves of experimental results of the composite at room temperature as well as FEA results are plotted with other results of bulk and lattice samples in Figure 15 and Figure 16 for compression and tension tests, respectively.

For the compression results, Young's modulus of the composite simulated by ABAQUS™ is more than the experimental one. This is because the pores inside the microstructure, and the incohesive bonding between the lattice and matrix by SLM, will decrease Young's modulus compared to the ideal case, which is supposed to be the reason for lower Young's modulus of the experimental curve. However, the calculated numerical deviation 2.0% for the ultimate compressive stress confirms that the FEA simulation shows a good accuracy. Besides, it is also apparent from the plot that the yielding and ultimate compressive strength has been significantly enhanced from the lattice shown in blue to the composite shown in black due to the filled-in matrix part. Nonetheless, the mechanical properties of the composite are less than the bulk aluminum properties shown in red. This can be addressed by increasing the volume fraction of the lattice. Using the rule of mixtures, this would result in composite properties between the lower bound of bulk aluminum and the upper bound of bulk 316L stainless steel.

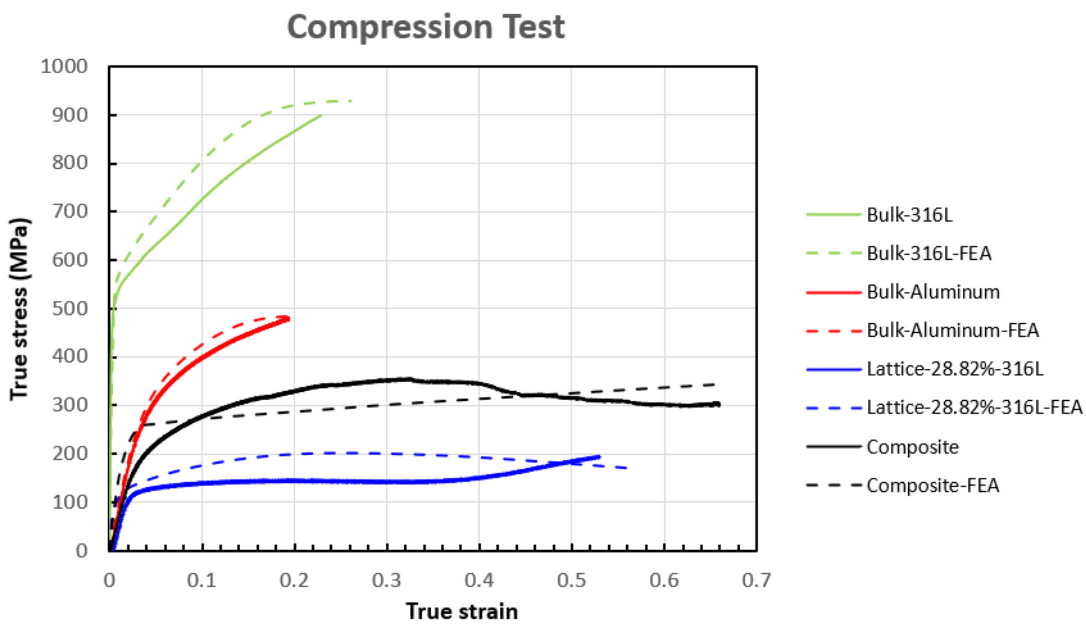

Figure 15. Comparison between experimental and FEA results of bulk 316L stainless steel, bulk dissolvable aluminum 316L stainless steel lattice, and 316L stainless steel/ dissolvable aluminum composite for the compression test.

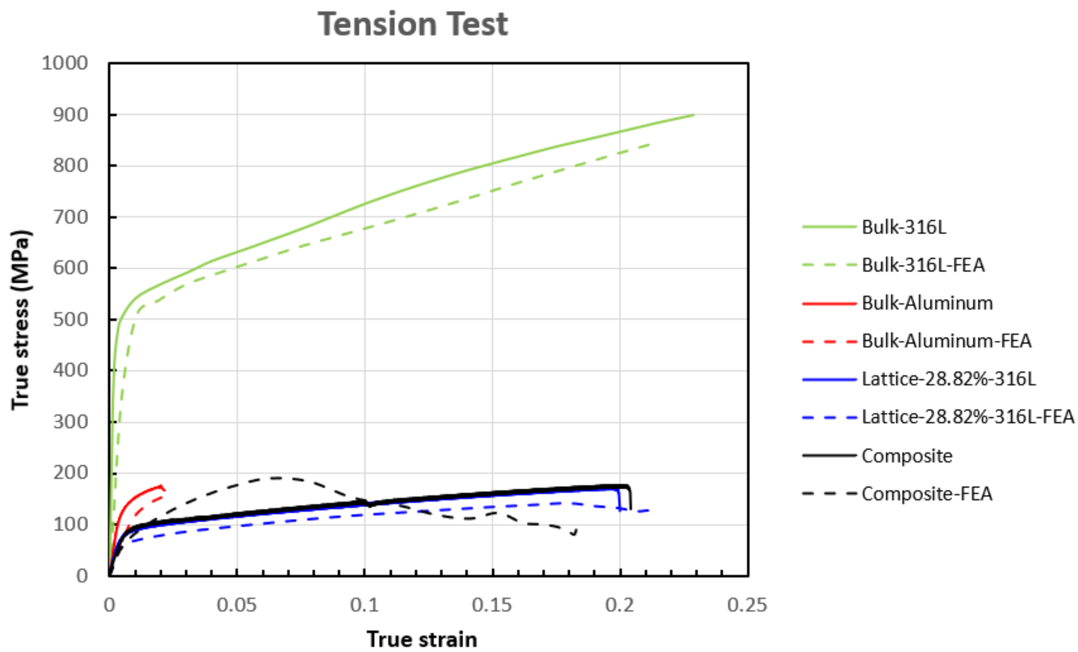

Figure 16. Comparison between experimental and FEA results of bulk 316L stainless steel, bulk dissolvable aluminum 316L stainless steel lattice, and 316L stainless steel/ dissolvable aluminum composite for the tension test.

Composite compression and tension experimental curves were taken out of the plots shown in Figure 17 and Figure 19. As clarified in Section 3.3, three unique points, namely the yielding point, the point in the plastic region, and the point in the hardening region, were marked out with their true strain and true stress values, and the corresponding frames captured by the DIC system were shown in Figure 18. In contrast, four special points, namely the yielding point, the point in the plastic region, the point before the first curve dip, and the last point that the DIC effectively tracked, were marked out, and the

DIC results were shown in **Figure 20**. The corresponding time calculated for the compression one was 35 s, 179 s, and 383 s, while 9 s, 21 s, 54 s, and 101 s for the tension one.

The tension results are different from the compression curves, where two distinct regions can be found in the experimental results, the elastic region, and plastic region, after which a sudden drop is shown, indicating the rupture of the sample. Besides, it is significantly noticeable that the tensile curves for the 316L stainless steel lattice and bimetallic lattice are similar. This indicates that the aluminum matrix does not play an essential role due to lack of bonding. Similar to the compression results, the bulk 316L stainless steel and bulk aluminum possess higher yield stress and ultimate tensile stress, and both tensile curves of the 316L lattice and composite do not even surpass the curve of bulk aluminum. However, the dissolvable aluminum presents a much lower elongation comparing to the other three samples. The trivial difference between the experimental and FEA data for all four pairs validates the simulation results, including the numerical calculated deviation of 2.0% for the ultimate stress of the tension composite. The ABAQUS simulation curve for the bimetallic composite generally matches the results from Cheng et al. [49].

4.3. Experimental validation with DIC results

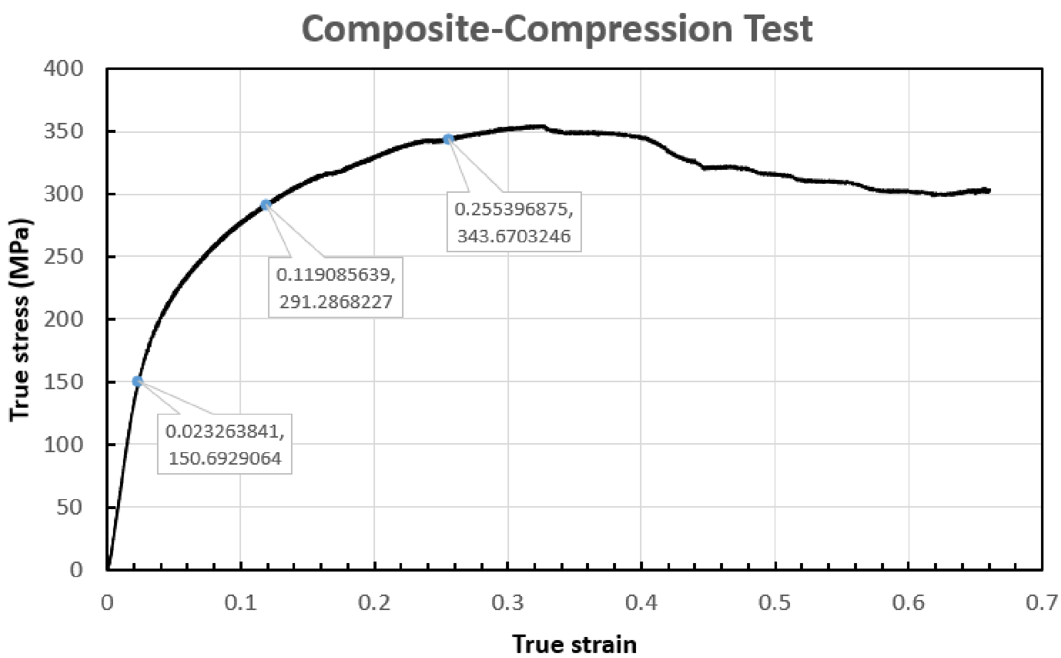

Figure 17. The experimental result of compression composite cube with three unique points marked out with *true stress* and *true strain*.

A strain range of -0.3 to 0 was exhibited in the compression and 0 to 0.1 in the tension. The strain behavior of the compression composite represented by the color coding was very similar to the bulk dissolvable aluminum; however, differences were observed for the tension composite. The strain growth was observed to grow gradually from the center to both sides, initially from 0 shown as purple color in the first frame to about 0.08 with orange color appearing in the middle part of the last frame. Experimental strain results of the curve plots match the value range plotted in the frames for both the compression and tension composite samples.

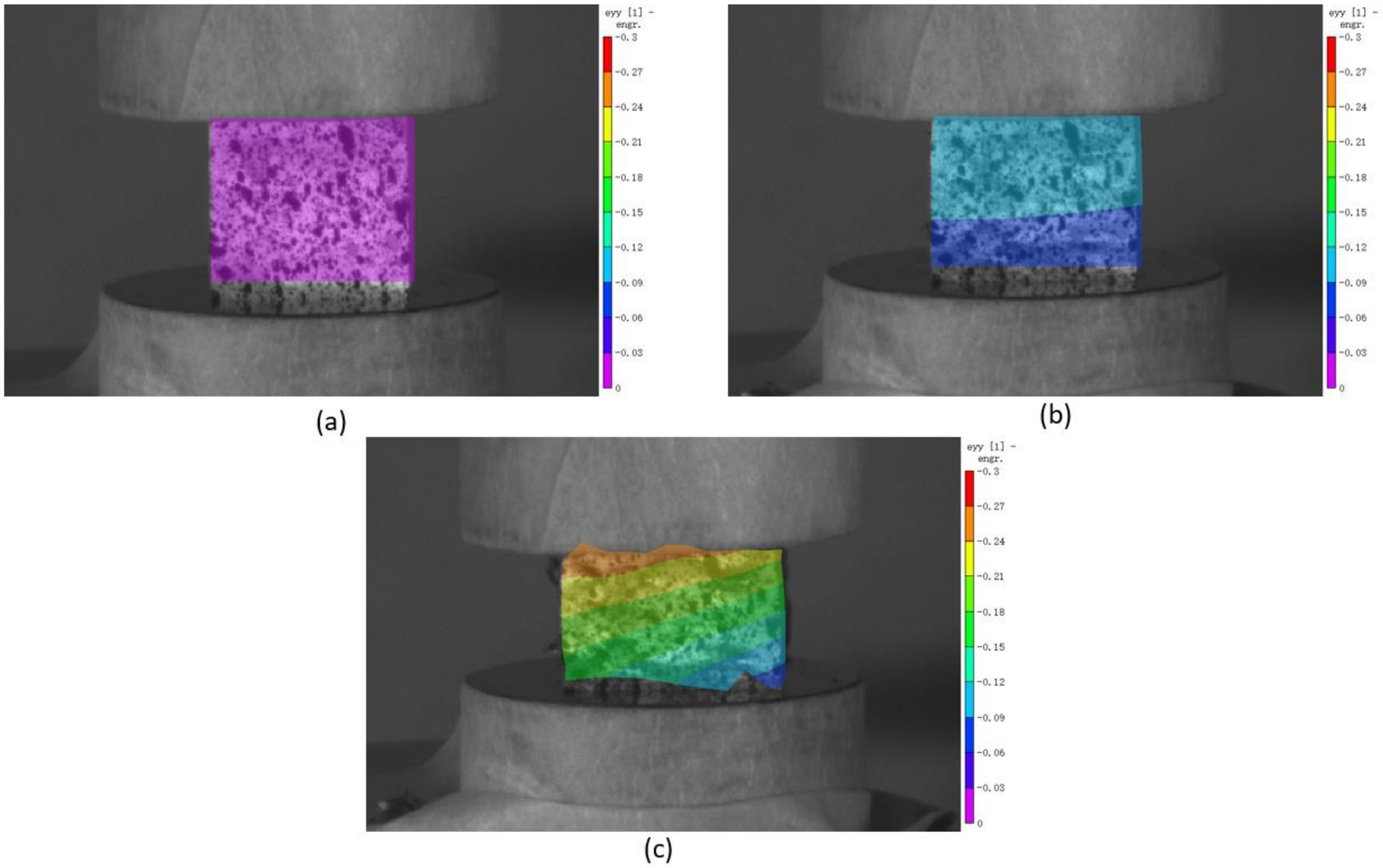

Figure 18. DIC frames of the three points marked out in the composite compression curve: (**a**) 35 s; (**b**) 179 s; (**c**) 383 s.

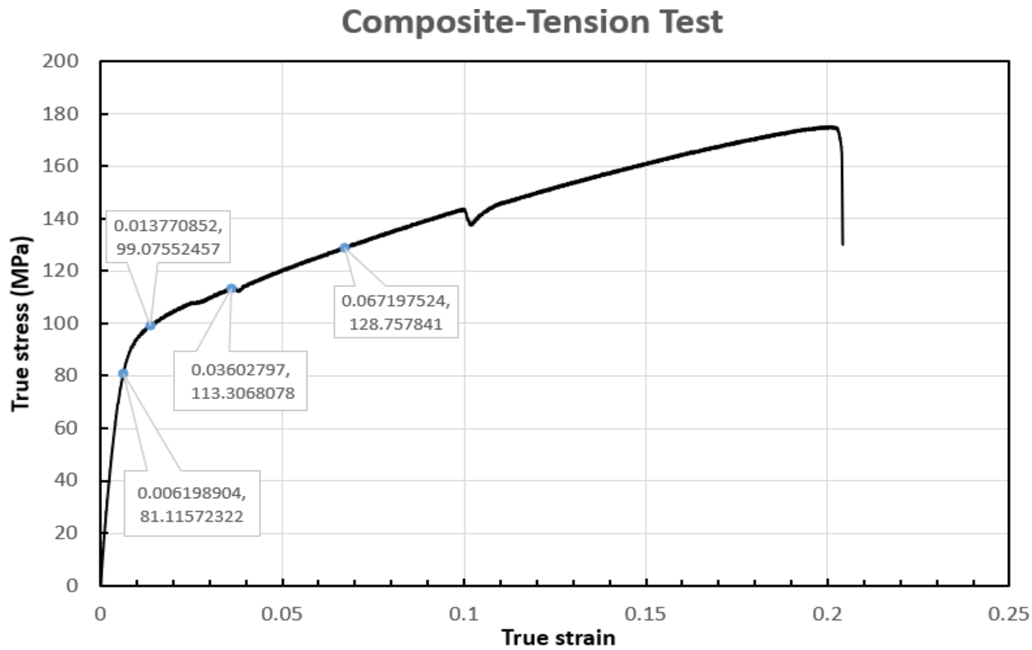

Figure 19. The experimental result of tension composite dog-bone with four unique points marked out with *true stress* and *true strain*.

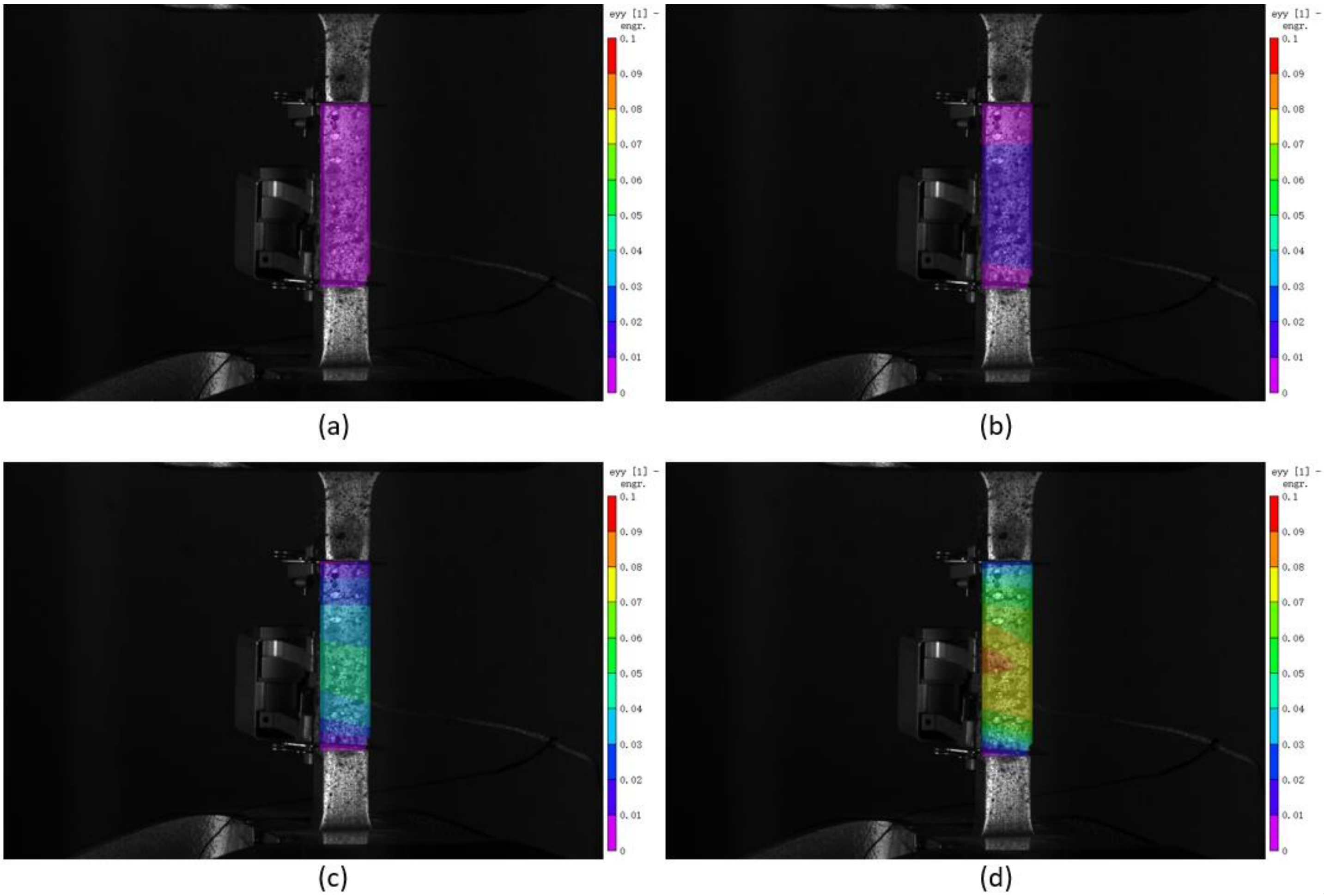

Figure 20. DIC frames of the four points marked out in the composite tension curve: (**a**) 9 s; (**b**) 21 s; (**c**) 54 s; (**d**) 101 s.

5. Conclusions

By investigating the compressive and tensile behaviour of 316L stainless steel lattice, bulk dissolvable aluminum, and 316L stainless steel/dissolvable aluminum bimetallic composite, the following conclusions can be obtained:

1) The developed FEA model is an acceptable simulation for the experimental work. After validating the effectiveness of ABAQUS™ FEA simulation on the current experiments, the simulation can be used to explore different volume fractions of base lattice and filler to obtain desired properties without the need for extensive experiments. For bulk and lattice samples, the average calculated numerical deviations between experimental and FEA results in this study for yield stress and ultimate stress are 9.8% and 5.0% for compressive tests and 2.1% and 8.9% for tensile tests, respectively. For composite samples, the average calculated numerical deviations for ultimate stress are 2.0% for both compressive and tensile experiments.

2) 316L stainless steel has better compressive properties and higher resistance to the tensile loading than dissolvable aluminum, which is much more brittle with less elongation.

3) In the tension test, due to lack of bonding, the load does not transfer from the 316L stainless steel lattice to aluminum alloy. However, the aluminum alloy part plays an indispensable role in the compression test and enhances the composite's compression strength compared to the lattice itself.

4) The elastic modulus, yielding stress, and ultimate stress of both the 316L stainless steel lattice and bimetallic composite were lower than the bulk aluminum, proving that the performance of the lattice and composite with a volume fraction of 28.82% is still

not that satisfactory. Increasing the strut diameter of lattice to achieve a higher volume fraction is expected to enhance the mechanical properties, including both compressive and tensile strengths.

Author Contributions: Data curation, formal analysis, investigation, software, validation, visualization, and writing-original draft preparation, X.L.; data curation, formal analysis, investigation, resources, validation, visualization, and writing-review and editing, M.G.K.; investigation, methodology, resources, supervision, validation, and writing-review and editing, A.A.B.; supervision, validation, and writing-review and editing, J.L.; conceptualization, funding acquisition, methodology, resources, supervision, validation, and writing-review and editing, H.H.; conceptualization, methodology, software, supervision, validation, and writing-review and editing, Z.C.; conceptualization, funding acquisition, methodology, project administration, resources, supervision, validation, and writing-review and editing, A.J.Q. All authors have read and agreed to the published version of the manuscript.

Funding: This research was funded by NSERC, grant number EGP 543505-19 Qureshi, and Alberta Innovates CASBE, grant number G2020000060 Q, and the APC was funded by the same grants.

Institutional Review Board Statement: Not applicable.

Informed Consent Statement: Not applicable.

Data Availability Statement: The study did not report any data.

Acknowledgments: The author thanks Alberta Innovations Corporation, the Natural Science and Engineering Research Council of Canada (NSERC), and Boss Completions Ltd for financial support, as well as Mr. Kelsey Kalinski of Boss Completions. Ltd. for valuable suggestions.

Conflicts of Interest: The authors declare that they have no known competing financial interests or personal relationships, which seem to affect the work reported in this article.

References

1. Yan, C., Hao, L., Hussein, A., Young, P., Raymont, D.: Advanced lightweight 316L stainless steel cellular lattice structures fabricated via selective laser melting. Mater. Des. 55, 533–541 (2014). https://doi.org/10.1016/j.matdes.2013.10.027
2. McKown, S., Shen, Y., Brookes, W.K., Sutcliffe, C.J., Cantwell, W.J., Langdon, G.S., Nurick, G.N., Theobald, M.D.: The quasi-static and blast loading response of lattice structures. Int. J. Impact Eng. 35, 795–810 (2008). https://doi.org/10.1016/j.ijimpeng.2007.10.005
3. Alsalla, H., Hao, L., Smith, C.: Fracture toughness and tensile strength of 316L stainless steel cellular lattice structures manufactured using the selective laser melting technique. Mater. Sci. Eng. A. 669, 1–6 (2016). https://doi.org/10.1016/j.msea.2016.05.075
4. Park, J.H., Park, K.: Compressive behavior of soft lattice structures and their application to functional compliance control. Addit. Manuf. 33, 101148 (2020). https://doi.org/10.1016/j.addma.2020.101148
5. Yánez, A., Herrera, A., Martel, O., Monopoli, D., Afonso, H.: Compressive behaviour of gyroid lattice structures for human cancellous bone implant applications. Mater. Sci. Eng. C. 68, 445–448 (2016). https://doi.org/10.1016/j.msec.2016.06.016
6. Kellogg, R.A., Russell, A.M., Lograsso, T.A., Flatau, A.B., Clark, A.E., Wun-Fogle, M.: Tensile properties of magnetostrictive iron-gallium alloys. Acta Mater. 52, 5043–5050 (2004). https://doi.org/10.1016/j.actamat.2004.07.007
7. Rossiter, J.D., Johnson, A.A., Bingham, G.A.: Assessing the Design and Compressive Performance of Material Extruded Lattice Structures. 3D Print. Addit. Manuf. 7, 19–27 (2020). https://doi.org/10.1089/3dp.2019.0030
8. Campanelli, S.L., Contuzzi, N., Ludovico, A.D., Caiazzo, F., Cardaropoli, F., Sergi, V.: Manufacturing and characterization of Ti6Al4V lattice components manufactured by selective laser melting. Materials (Basel). 7, 4803–4822 (2014). https://doi.org/10.3390/ma7064803
9. Liu, L., Kamm, P., García-Moreno, F., Banhart, J., Pasini, D.: Elastic and failure response of imperfect three-dimensional metallic lattices: the role of geometric defects induced by Selective Laser Melting. J. Mech. Phys. Solids. 107, 160–184 (2017). https://doi.org/10.1016/j.jmps.2017.07.003
10. Geng, L., Wu, W., Sun, L., Fang, D.: Damage characterizations and simulation of selective laser melting fabricated 3D re-entrant lattices based on in-situ CT testing and geometric reconstruction. Int. J. Mech. Sci. 157–158, 231–242 (2019). https://doi.org/10.1016/j.ijmecsci.2019.04.054
11. Zargarian, A., Esfahanian, M., Kadkhodapour, J., Ziaei-Rad, S., Zamani, D.: On the fatigue behavior of additive manufactured lattice structures. Theor. Appl. Fract. Mech. 100, 225–232 (2019). https://doi.org/10.1016/j.tafmec.2019.01.012
12. Peng, C., Tran, P., Nguyen-Xuan, H., Ferreira, A.J.M.: Mechanical performance and fatigue life prediction of lattice structures: Parametric computational approach. Compos. Struct. 235, 111821 (2020). https://doi.org/10.1016/j.compstruct.2019.111821

13. Moongkhamklang, P., Deshpande, V.S., Wadley, H.N.G.: The compressive and shear response of titanium matrix composite lattice structures. Acta Mater. 58, 2822–2835 (2010). https://doi.org/10.1016/j.actamat.2010.01.004
14. De Wild, M., Ghayor, C., Zimmermann, S., Rüegg, J., Nicholls, F., Schuler, F., Chen, T.H., Weber, F.E.: Osteoconductive Lattice Microarchitecture for Optimized Bone Regeneration. 3D Print. Addit. Manuf. 6, 40–49 (2019). https://doi.org/10.1089/3dp.2017.0129
15. Egan, P., Wang, X., Greutert, H., Shea, K., Wuertz-Kozak, K., Ferguson, S.: Mechanical and Biological Characterization of 3D Printed Lattices. 3D Print. Addit. Manuf. 6, 73–81 (2019). https://doi.org/10.1089/3dp.2018.0125
16. Melancon, D., Bagheri, Z.S., Johnston, R.B., Liu, L., Tanzer, M., Pasini, D.: Mechanical characterization of structurally porous biomaterials built via additive manufacturing: experiments, predictive models, and design maps for load-bearing bone replacement implants. Acta Biomater. 63, 350–368 (2017). https://doi.org/10.1016/j.actbio.2017.09.013
17. Al-Ketan, O., Lee, D.W., Rowshan, R., Abu Al-Rub, R.K.: Functionally graded and multi-morphology sheet TPMS lattices: Design, manufacturing, and mechanical properties. J. Mech. Behav. Biomed. Mater. 102, 103520 (2020). https://doi.org/10.1016/j.jmbbm.2019.103520
18. Liu, F., Mao, Z., Zhang, P., Zhang, D.Z., Jiang, J., Ma, Z.: Functionally graded porous scaffolds in multiple patterns: New design method, physical and mechanical properties. Mater. Des. 160, 849–860 (2018). https://doi.org/10.1016/j.matdes.2018.09.053
19. Li, D., Liao, W., Dai, N., Dong, G., Tang, Y., Xie, Y.M.: Optimal design and modeling of gyroid-based functionally graded cellular structures for additive manufacturing. CAD Comput. Aided Des. 104, 87–99 (2018). https://doi.org/10.1016/j.cad.2018.06.003
20. Azzouz, L., Chen, Y., Zarrelli, M., Pearce, J.M., Mitchell, L., Ren, G., Grasso, M.: Mechanical properties of 3-D printed truss-like lattice biopolymer non-stochastic structures for sandwich panels with natural fibre composite skins. Compos. Struct. 213, 220–230 (2019). https://doi.org/10.1016/j.compstruct.2019.01.103
21. Fan, H., Yang, W., Bin, W., Yan, Y., Qiang, F., Zhuang, Z.: TSINGHUA SCIENCE AND TECHNOLOGY I S S N 1 0 0 7 -0 2 1 4 0 4 / 1 8 p Design and Manufacturing of a Composite Lattice Structure Reinforced by Continuous Carbon Fibers. Tsinghua Sci. Technol. 5, 1–5 (2006)
22. Ye, G., Bi, H., Chen, L., Hu, Y.: Compression and Energy Absorption Performances of 3D Printed Polylactic Acid Lattice Core Sandwich Structures. 3D Print. Addit. Manuf. 6, 333–343 (2019). https://doi.org/10.1089/3dp.2019.0068
23. Arabnejad, S., Pasini, D.: Mechanical properties of lattice materials via asymptotic homogenization and comparison with alternative homogenization methods. Int. J. Mech. Sci. 77, 249–262 (2013). https://doi.org/10.1016/j.ijmecsci.2013.10.003
24. Wang, Y., Xu, H., Pasini, D.: Multiscale isogeometric topology optimization for lattice materials. Comput. Methods Appl. Mech. Eng. 316, 568–585 (2017). https://doi.org/10.1016/j.cma.2016.08.015
25. Andersen, M.N., Wang, F., Sigmund, O.: On the competition for ultimately stiff and strong architected materials. arXiv. (2020)
26. Alzahrani, M., Choi, S.K., Rosen, D.W.: Design of truss-like cellular structures using relative density mapping method. Mater. Des. 85, 349–360 (2015). https://doi.org/10.1016/j.matdes.2015.06.180
27. Ai, L., Gao, X.L.: Metamaterials with negative Poisson's ratio and non-positive thermal expansion. Compos. Struct. 162, 70–84 (2017). https://doi.org/10.1016/j.compstruct.2016.11.056
28. Deng, F., Nguyen, Q.K., Zhang, P.: Multifunctional liquid metal lattice materials through hybrid design and manufacturing. Addit. Manuf. 33, 101117 (2020). https://doi.org/10.1016/j.addma.2020.101117
29. Maconachie, T., Leary, M., Lozanovski, B., Zhang, X., Qian, M., Faruque, O., Brandt, M.: SLM lattice structures: Properties, performance, applications and challenges. Mater. Des. 183, 108137 (2019). https://doi.org/10.1016/j.matdes.2019.108137
30. Köhnen, P., Haase, C., Bültmann, J., Ziegler, S., Schleifenbaum, J.H., Bleck, W.: Mechanical properties and deformation behavior of additively manufactured lattice structures of stainless steel. Mater. Des. 145, 205–217 (2018). https://doi.org/10.1016/j.matdes.2018.02.062
31. Contuzzi, N., Campanelli, S.L., Casavola, C., Lamberti, L.: Manufacturing and characterization of 18Ni marage 300 lattice components by selective laser melting. Materials (Basel). 6, 3451–3468 (2013). https://doi.org/10.3390/ma6083451
32. O.Rehme, C.Emmelmann, D.S.: Selective Laser Melting of lattice structures in solid shells. (1970)
33. Hanzl, P., Zetková, I., Daňa, M.: Uniaxial tensile load of lattice structures produced by metal additive manufacturing. Manuf. Technol. 19, 228–231 (2019). https://doi.org/10.21062/ujep/274.2019/a/1213-2489/mt/19/2/228
34. Li, C., Lei, H., Liu, Y., Zhang, X., Xiong, J., Zhou, H., Fang, D.: Crushing behavior of multi-layer metal lattice panel fabricated by selective laser melting. Int. J. Mech. Sci. 145, 389–399 (2018). https://doi.org/10.1016/j.ijmecsci.2018.07.029
35. Sola, A., Defanti, S., Mantovani, S., Merulla, A., Denti, L.: Technological Feasibility of Lattice Materials by Laser-Based Powder Bed Fusion of A357.0. 3D Print. Addit. Manuf. 7, 1–7 (2020). https://doi.org/10.1089/3dp.2019.0119
36. Peto, M., Ramirez-Cedillo, E., Uddin, M.J., Rodriguez, C.A., Siller, H.R.: Mechanical behavior of lattice structures fabricated by direct light processing with compression testing and size optimization of unit cells. ASME Int. Mech. Eng. Congr. Expo. Proc. 3, 1–10 (2019). https://doi.org/10.1115/IMECE2019-12260
37. Dallago, M., Zanini, F., Carmignato, S., Pasini, D., Benedetti, M.: Effect of the geometrical defectiveness on the mechanical properties of SLM biomedical Ti6Al4V lattices. Procedia Struct. Integr. 13, 161–167 (2018). https://doi.org/10.1016/j.prostr.2018.12.027
38. El Elmi, A., Melancon, D., Asgari, M., Liu, L., Pasini, D.: Experimental and numerical investigation of selective laser melting-induced defects in Ti-6Al-4V octet truss lattice material: The role of material microstructure and morphological variations. J. Mater. Res. 1–13 (2020). https://doi.org/10.1557/jmr.2020.75

39. Dallago, M., Raghavendra, S., Luchin, V., Zappini, G., Pasini, D., Benedetti, M.: Geometric assessment of lattice materials built via Selective Laser Melting. Mater. Today Proc. 7, 353–361 (2019). https://doi.org/10.1016/j.matpr.2018.11.096
40. Sharma, P., Pandey, P.M.: Morphological and mechanical characterization of topologically ordered open cell porous iron foam fabricated using 3D printing and pressureless microwave sintering. Mater. Des. 160, 442–454 (2018). https://doi.org/10.1016/j.matdes.2018.09.029
41. Dressler, A.D., Jost, E.W., Miers, J.C., Moore, D.G., Seepersad, C.C., Boyce, B.L.: Heterogeneities dominate mechanical performance of additively manufactured metal lattice struts. Addit. Manuf. 28, 692–703 (2019). https://doi.org/10.1016/j.addma.2019.06.011
42. Bagheri, Z.S., Melancon, D., Liu, L., Johnston, R.B., Pasini, D.: Compensation strategy to reduce geometry and mechanics mismatches in porous biomaterials built with Selective Laser Melting. J. Mech. Behav. Biomed. Mater. 70, 17–27 (2017). https://doi.org/10.1016/j.jmbbm.2016.04.041
43. Tsopanos, S., Mines, R.A.W., McKown, S., Shen, Y., Cantwell, W.J., Brooks, W., Sutcliffe, C.J.: The influence of processing parameters on the mechanical properties of selectively laser melted stainless steel microlattice structures. J. Manuf. Sci. Eng. Trans. ASME. 132, 0410111–04101112 (2010). https://doi.org/10.1115/1.4001743
44. Seepersad, C.C., Allison, J.A., Dressler, A.D., Boyce, B.L., Kovar, D.: An experimental approach for enhancing the predictability of mechanical properties of additively manufactured architected materials with manufacturing-induced variability. Elsevier Ltd (2020)
45. Hengsbach, F., Koppa, P., Duschik, K., Holzweissig, M.J., Burns, M., Nellesen, J., Tillmann, W., Tröster, T., Hoyer, K.P., Schaper, M.: Duplex stainless steel fabricated by selective laser melting - Microstructural and mechanical properties. Mater. Des. 133, 136–142 (2017). https://doi.org/10.1016/j.matdes.2017.07.046
46. Zhong, T., He, K., Li, H., Yang, L.: Mechanical properties of lightweight 316L stainless steel lattice structures fabricated by selective laser melting. Mater. Des. 181, 108076 (2019). https://doi.org/10.1016/j.matdes.2019.108076
47. Zhang, M., Yang, Y., Wang, D., Song, C., Chen, J.: Microstructure and mechanical properties of CuSn/18Ni300 bimetallic porous structures manufactured by selective laser melting. Mater. Des. 165, 107583 (2019). https://doi.org/10.1016/j.matdes.2019.107583
48. Pawlowski, A.E., Cordero, Z.C., French, M.R., Muth, T.R., Keith Carver, J., Dinwiddie, R.B., Elliott, A.M., Shyam, A., Splitter, D.A.: Damage-tolerant metallic composites via melt infiltration of additively manufactured preforms. Mater. Des. 127, 346–351 (2017). https://doi.org/10.1016/j.matdes.2017.04.072
49. J. Cheng, M. Gussev, J. Allen, et al.: Deformation and failure of PrintCast A356/316 L composites: Digital image correlation and finite element modeling. BBA - Biomembr. 183135 (2019). https://doi.org/10.1016/j.bbamem.2019.183135
50. Xu, W., Yu, A., Lu, X., Tamaddon, M., Wang, M., Zhang, J., Zhang, J., Qu, X., Liu, C., Su, B.: Design and performance evaluation of additively manufactured composite lattice structures of commercially pure Ti (CP–Ti). Bioact. Mater. 6, 1215–1222 (2021). https://doi.org/10.1016/j.bioactmat.2020.10.005
51. McDonald-Wharry, J., Amirpour, M., Pickering, K.L., Battley, M., Fu, Y.: Moisture sensitivity and compressive performance of 3D-printed cellulose-biopolyester foam lattices. Addit. Manuf. 40, 101918 (2021). https://doi.org/10.1016/j.addma.2021.101918
52. Mahmoud, D., Al-Rubaie, K.S., Elbestawi, M.A.: The influence of selective laser melting defects on the fatigue properties of Ti6Al4V porosity graded gyroids for bone implants. Int. J. Mech. Sci. 193, (2021). https://doi.org/10.1016/j.ijmecsci.2020.106180
53. Feng, J., Liu, B., Lin, Z., Fu, J.: Isotropic octet-truss lattice structure design and anisotropy control strategies for implant application. Mater. Des. 203, 109595 (2021). https://doi.org/10.1016/j.matdes.2021.109595
54. Traxel, K.D., Groden, C., Valladares, J., Bandyopadhyay, A.: Mechanical properties of additively manufactured variable lattice structures of Ti6Al4V. Mater. Sci. Eng. A. 809, 140925 (2021). https://doi.org/10.1016/j.msea.2021.140925
55. Hajjari, M., Jafari Nedoushan, R., Dastan, T., Sheikhzadeh, M., Yu, W.R.: Lightweight weft-knitted tubular lattice composite for energy absorption applications: An experimental and numerical study. Int. J. Solids Struct. 213, 77–92 (2021). https://doi.org/10.1016/j.ijsolstr.2020.12.017
56. Li, P.Y., Ma, Y.E., Sun, W.B., Qian, X., Zhang, W., Wang, Z.H.: Fracture and failure behavior of additive manufactured Ti6Al4V lattice structures under compressive load. Eng. Fract. Mech. 244, (2021). https://doi.org/10.1016/j.engfracmech.2021.107537
57. Cao, X., Xiao, D., Li, Y., Wen, W., Zhao, T., Chen, Z., Jiang, Y., Fang, D.: Dynamic compressive behavior of a modified additively manufactured rhombic dodecahedron 316L stainless steel lattice structure. Thin-Walled Struct. 148, 106586 (2020). https://doi.org/10.1016/j.tws.2019.106586
58. Xiao, L., Song, W., Xu, X.: Experimental study on the collapse behavior of graded Ti-6Al-4V micro-lattice structures printed by selective laser melting under high speed impact. Thin-Walled Struct. 155, 106970 (2020). https://doi.org/10.1016/j.tws.2020.106970
59. Goodall, R., Hernandez-Nava, E., Jenkins, S.N.M., Sinclair, L., Tyrwhitt-Jones, E., Khodadadi, M.A., Ip, D.H., Ghadbeigi, H.: The effects of defects and damage in the mechanical behavior of ti6al4v lattices. Front. Mater. 6, 1–11 (2019). https://doi.org/10.3389/fmats.2019.00117
60. Liu, F., Zhang, D.Z., Zhang, P., Zhao, M., Jafar, S.: Mechanical properties of optimized diamond lattice structure for bone scaffolds fabricated via selective laser melting. Materials (Basel). 11, (2018). https://doi.org/10.3390/ma11030374
61. Xiao, L., Song, W.: Additively-manufactured functionally graded Ti-6Al-4V lattice structures with high strength under static and dynamic loading: Experiments. Int. J. Impact Eng. 111, 255–272 (2018). https://doi.org/10.1016/j.ijimpeng.2017.09.018

62. Montanini, R., Rossi, G., Quattrocchi, A., Alizzio, D., Capponi, L., Marsili, R., Giacomo, A. Di, Tocci, T.: Structural characterization of complex lattice parts by means of optical non-contact measurements. I2MTC 2020 - Int. Instrum. Meas. Technol. Conf. Proc. 1–6 (2020). https://doi.org/10.1109/I2MTC43012.2020.9128771
63. Hao, W., Liu, Y., Wang, T., Guo, G., Chen, H., Fang, D.: Failure analysis of 3D printed glass fiber/PA12 composite lattice structures using DIC. Compos. Struct. 225, 111192 (2019). https://doi.org/10.1016/j.compstruct.2019.111192
64. Fíla, T., Koudelka, P., Falta, J., Zlámal, P., Rada, V., Adorna, M., Bronder, S., Jiroušek, O.: Dynamic impact testing of cellular solids and lattice structures: Application of two-sided direct impact Hopkinson bar. Int. J. Impact Eng. 148, (2021). https://doi.org/10.1016/j.ijimpeng.2020.103767
65. Li, S., Hu, M., Xiao, L., Song, W.: Compressive properties and collapse behavior of additively-manufactured layered-hybrid lattice structures under static and dynamic loadings. Thin-Walled Struct. 157, 107153 (2020). https://doi.org/10.1016/j.tws.2020.107153
66. ASTM E8: ASTM E8/E8M standard test methods for tension testing of metallic materials 1. Annu. B. ASTM Stand. 4. 1–27 (2010). https://doi.org/10.1520/E0008
67. Ghasri-Khouzani, M., Li, X., Bogno, A.A., Liu, J., Henein H., Chen, Z., Qureshi, A.J.: Investigation of compressive and tensile behavior of stainless steel/dissolvable aluminum bimetallic composites by finite element modelling and digital image correlation [Manuscript submitted for publication].
68. ◌ABAQUS: Abaqus 6.14. Abaqus 6.14 Anal. User's Guid. 14 (2014)
69. Lombard, M.: Introducing SolidWorks. SolidWorks® 2011 Parts Bible. 1–35 (2013). https://doi.org/10.1002/9781118257753.ch1
70. Mower, T.M., Long, M.J.: Mechanical behavior of additive manufactured, powder-bed laser-fused materials. Mater. Sci. Eng. A. 651, 198–213 (2016). https://doi.org/10.1016/j.msea.2015.10.068